Research Article | Vol. 26, No. 10 | 14 May 2018 | OPTICS EXPRESS A360
Optics EXPRESS

Effect of non-stoichiometry on optical, radiative, and thermal characteristics of ceria undergoing reduction

VINCENT M. WHEELER, JOSÉ I. ZAPATA, PETER B. KREIDER, AND WOJCIECH LIPIŃSKI*

Research School of Engineering, The Australian National University, Canberra, ACT 2602, Australia
**wojciech.lipinski@anu.edu.au*

Abstract: The complex refractive index of ceria has been determined at ambient temperature using variable angle spectroscopic ellipsometry for two chemical states—fully oxidized and partially reduced. The ellipsometric model is corroborated with complementary measurements of thickness, surface roughness, and chemical composition. Partially reduced ceria is shown to have a larger absorption index over a broad spectral range than fully oxidized ceria, including the visible and near IR regions. We use a simple model of a directly irradiated particle entrained in a gas flow to demonstrate the consequences of accounting for changes in chemical state when modeling ceria-based thermochemical process.

OCIS codes: (350.5340) Photothermal effects; (350.6050) Solar energy; (310.6860) Thin films, optical properties.

References and links

1. W. C. Chueh and S. M. Haile, "A thermochemical study of ceria: exploiting an old material for new modes of energy conversion and CO_2 mitigation," Philos. Trans. A Math. Phys. Eng. Sci. **368**(1923), 3269–3294 (2010).
2. W. C. Chueh, C. Falter, M. Abbott, D. Scipio, P. Furler, S. M. Haile, and A. Steinfeld, "High-flux solar-driven thermochemical dissociation of CO_2 and H_2O using nonstoichiometric ceria," Science **330**(6012), 1797–1801 (2010).
3. J. R. Scheffe and A. Steinfeld, "Oxygen exchange materials for solar thermochemical splitting of H_2O and CO_2: A review," Mater. Today **17**(7), 341–348 (2014).
4. D. Marxer, P. Furler, M. Takacs, and A. Steinfeld, "Solar thermochemical splitting of CO_2 into separate streams of CO and O_2 with high selectivity, stability, conversion, and efficiency," Energy Environ. Sci. **10**(5), 1142–1149 (2017).
5. P. T. Krenzke and J. H. Davidson, "On the efficiency of solar H_2 and CO production via the thermochemical cerium oxide redox cycle: The option of inert-swept reduction," Energy Fuels **29**(2), 1045–1054 (2015).
6. S. Ackermann, J. R. Scheffe, and A. Steinfeld, "Diffusion of oxygen in ceria at elevated temperatures and its application to H_2O/CO_2 splitting thermochemical redox cycles," J. Phys. Chem. C **118**(10), 5216–5225 (2014).
7. K. Ganesan, L. A. Dombrovsky, T.-S. Oh, and W. Lipiński, "Determination of optical constants of ceria by combined analytical and experimental approaches," JOM **65**(12), 1694–1701 (2013).
8. P. Patsalas, S. Logothetidis, and C. Metaxa, "Optical performance of nanocrystalline transparent ceria films," Appl. Phys. Lett. **81**(3), 466–468 (2002).
9. S. Guo, H. Arwin, S. N. Jacobsen, K. Järrendahl, and U. Helmersson, "A spectroscopic ellipsometry study of cerium dioxide thin films grown on sapphire by RF magnetron sputtering," J. Appl. Phys. **77**(10), 5369–5376 (1995).
10. G. Balakrishnan, S. T. Sundari, P. Kuppusami, P. C. Mohan, M. P. Srinivasan, E. Mohandas, V. Ganesan, and D. Sastikumar, "A study of microstructural and optical properties of nanocrystalline ceria thin films prepared by pulsed laser deposition," Thin Solid Films **519**(8), 2520–2526 (2011).
11. A. S. Oles and G. S. Jackson, "Modeling of a concentrated-solar, falling-particle receiver for ceria reduction," Sol. Energy **122**, 126–147 (2015).
12. A. J. Groehn, A. Lewandowski, R. Yang, and A. W. Weimer, "Hybrid radiation modeling for multi-phase solar-thermal reactor systems operated at high-temperature," Sol. Energy **140**, 130–140 (2016).
13. R. Bala Chandran, R. Bader, and W. Lipiński, "Transient heat and mass transfer analysis in a porous ceria structure of a novel solar redox reactor," Int. J. Therm. Sci. **92**, 138–149 (2015).
14. D. J. Keene, J. H. Davidson, and W. Lipiński, "A model of transient heat and mass transfer in a heterogeneous medium of ceria undergoing nonstoichiometric reduction," J. Heat Transfer **135**(5), 052701 (2013).
15. F. Marabelli and P. Wachter, "Covalent insulator CeO_2: Optical reflectivity measurements," Phys. Rev. B Condens. Matter **36**(2), 1238–1243 (1987).
16. R. J. Panlener, R. N. Blumenthal, and J. E. Garnier, "A thermodynamic study of nonstoichiometric cerium

#319880 https://doi.org/10.1364/OE.26.00A360
Journal © 2018 Received 16 Jan 2018; revised 8 Mar 2018; accepted 8 Mar 2018; published 19 Mar 2018

dioxide," Solid State Commun. **17**(1), iv–v (1975).
17. D. V. Likhachev, N. Malkova, and L. Poslavsky, "Modified Tauc–Lorentz dispersion model leading to a more accurate representation of absorption features below the bandgap," Thin Solid Films **589**, 844–851 (2015).
18. J. A. Woollam Co., "CompleteEASE Data Analysis Manual, Version 3.65," (2008).
19. S. Mohan and M. G. Krishna, "A review of ion beam assisted deposition of optical thin films," Vacuum **46**(7), 645–659 (1995).
20. A. H. Morshed, M. E. Moussa, S. M. Bedair, R. Leonard, S. X. Liu, and N. El-Masry, "Violet/blue emission from epitaxial cerium oxide films on silicon substrates," Appl. Phys. Lett. **70**(13), 1647–1649 (1997).
21. B. Bulfin, A. J. Lowe, K. A. Keogh, B. E. Murphy, O. Lü, S. A. Krasnikov, and I. V. Shvets, "Analytical model of CeO_2 oxidation and reduction," J. Mater. Chem. C Mater. Opt. Electron. Devices **117**, 24129–24137 (2013).
22. M. J. Moran, H. N. Shapiro, D. D. Boettner, and M. B. Bailey, *Fundamentals of Engineering Thermodynamics* (Wiley, 2010).
23. K. J. Daun and S. C. Huberman, "Influence of particle curvature on transition regime heat conduction from aerosolized nanoparticles," Int. J. Heat Mass Transf. **55**(25-26), 7668–7676 (2012).
24. I. Riess, M. Ricken, and J. Nölting, "On the specific heat of nonstoichiometric ceria," J. Solid State Chem. **57**(3), 314–322 (1985).
25. E. W. Lemmon and R. T. Jacobsen, "Viscosity and thermal conductivity equations for nitrogen, oxygen, argon, and air," Int. J. Thermophys. **25**(1), 21–69 (2004).
26. P. Thomas, *Simulation of Industrial Processes for Control Engineers* (Butterworth-Heinemann, 1999).
27. ASTM International, *References Solar Spectral Irradiance at Air Mass 1.5: Direct Normal and Hemispherical for a 37° Tilted Surface 1* (2004), Vol. 14.
28. J. Martinek, C. Bingham, and A. W. Weimer, "Computational modeling of a multiple tube solar reactor with specularly reflective cavity walls. Part 2: Steam gasification of carbon," Chem. Eng. Sci. **81**, 285–297 (2012).
29. T. M. Francis, C. Perkins, and A. W. Weimer, "Manganese oxide dissociation kinetics for the Mn_2O_3 thermochemical water-splitting cycle. Part 2: CFD model," Chem. Eng. Sci. **65**(15), 4397–4410 (2010).
30. S. K. Loyalka, "Mechanics of aerosols in nuclear reactor safety: A review," Prog. Nucl. Energy **12**(1), 1–56 (1983).
31. C. F. Bohren and D. R. Huffman, *Absorption and Scattering of Light by Small Particles* (Wiley, 2004).
32. L. Li, J. Coventry, R. Bader, J. Pye, and W. Lipiński, "Optics of solar central receiver systems: A review," Opt. Express **24**(14), A985–A1007 (2016).

1. Introduction

Cerium(IV) dioxide (ceria) has garnered recent attention as a promising exchange material for high-temperature thermal processing, particularly for synthetic fuel production [1,2]. The low efficiency of reactor systems employing non-stoichiometric ceria redox cycling to is a fundamental barrier to making it commercially viable [3]. Reaction systems utilizing ceria undergo a highly endothermic, non-stoichiometric reduction according to

$$\mathrm{CeO_2} \rightarrow \mathrm{CeO_{2-\delta}} + \frac{\delta}{2}\mathrm{O_2}, \tag{1}$$

where δ is the non-stoichiometry. To drive this reaction, the proof-of-concept ceria solar thermochemical reactor ran at temperatures up to 1640°C and with oxygen partial pressure of 10^{-5} atm [2]. Radiative losses can dominate energy efficiency at such temperatures where long dwell times combine with low chemical output to result in peak reported efficiency of just over 5% [4] despite theoretical efficiencies reported as high as 40% [5]. Previous work has found that the reaction rate and oxygen transport rate are not the rate-limiting mechanism for the reduction of ceria in certain size regimes; it is the heat transfer rate [6]. Thus, a detailed understanding of the radiative heat transfer in a solar reactor and to the reaction site is essential for the design of efficient solar thermochemical reactors.

The complex refractive index and morphology are required to determine radiative properties of a medium, which in turn are needed for radiative transfer analysis. Numerous studies have been carried out to determine the optical properties of stoichiometric ceria (e.g [7]. and literature

Optics EXPRESS

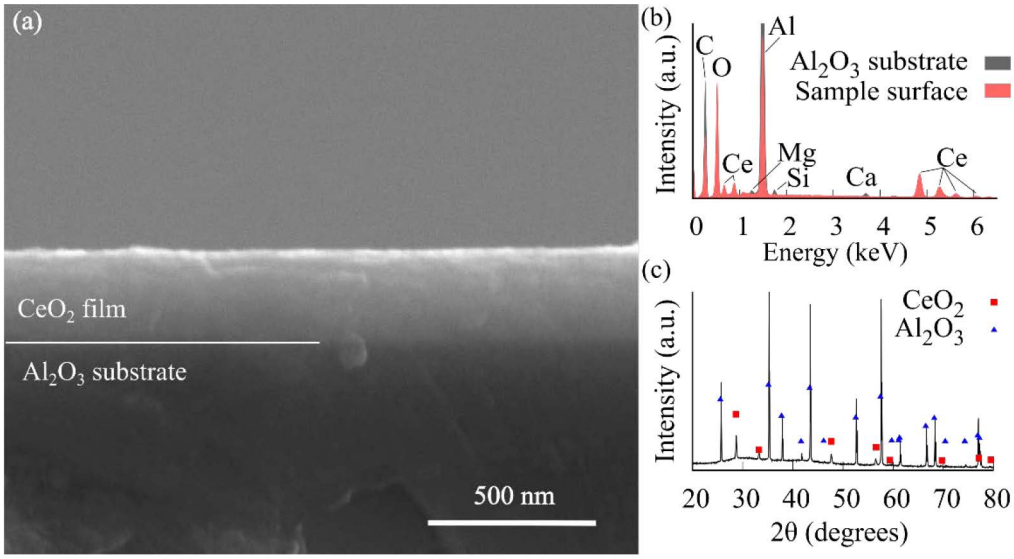

Fig. 1. CeO_2 thin film characterization. (a) Edge-on SEM image of the CeO_2 thin film on the Al_2O_3 substrate. (b) EDS analysis of the Al_2O_3 substrate in the edge-on SEM image and of the deposited CeO_2 film from the top down. (c) XRD pattern of the oxidized sample.

cited therein), including those for ceria deposited as a thin film and using variable angle spectroscopic ellipsometry (VASE) [8–10]. The refractive index is expected to be highly sensitive to the reduction state of the material since oxygen vacancies change the electronic structure of the material and can dramatically change the way the material responds to electromagnetic excitation. However, a rigorous study of the refractive index of ceria as a function of the reduction extent is yet to be published. Numerous computational studies have appeared recently to evaluate the design of ceria-based thermochemical reactors, for example [11–14], and the refractive index of ceria has been assumed independent of a chemical state. The present work therefore investigates the changes in refractive index of ceria as a function of reduction extent, then endeavors to illustrate its importance in modeling the performance of thermochemical reactor designs using a simple model.

2. Experimental determination of ceria radiative properties

Thin films of ceria were deposited, thermo-chemically processed, then chemically and morphologically characterized before determining the complex refractive index using VASE. We detail the experimental procedures and results in the following.

2.1 Sample preparation

Alumina (Al_2O_3) substrates 8 mm diameter and 1 mm thick with a polished surface (Coorstek ADS996) were chosen for the chemical inertness, high melting point, and coefficient of thermal expansion similar to ceria. Arithmetic average surface roughness of the polished sample was reported to be R_a<26 nm by the manufacturer. Pellets of 99.9% pure cerium (IV) oxide were evaporated using a Temescal BJD-2000 electronic beam physical vapor deposition system at a pressure of 6.7×10^{-10} bar to deposit a thin ceria film with a targeted thickness of approximately 100 nm. The material deposition rate was 1 Å s^{-1} with an electron beam current of approximately 25 A. No effort was made to control the temperature of the substrates during deposition. Cerium oxide pellets appeared near black after the deposition process suggesting substantial reduction as was observed in [15]. Therefore, samples were heat treated for 3 hours in a radiative furnace at 600°C under a flow of high-purity oxygen to obtain a fully oxidized sample. One sample was further heat treated in an environment with a

Optics EXPRESS

high-purity ($p_{O_2} \approx 10^{-6}$ bar) argon sweep gas at 1265°C for one hour to obtain a partially reduced state of ceria. These samples will be referred to as the oxidized and reduced samples, respectively. Diffusion rates of oxygen from ceria under similar conditions suggest that one hour reduction time is sufficient for the film to reach an equilibrium thermodynamic state [6]. We estimate the reduction state of ceria to correspond to a non-stoichiometry coefficient of 0.0144 from the thermodynamic data found in [16]. Quantitative spectroscopic determination of the reduction state is planned for future work.

2.2 Characterization

Field emission scanning electron microscope images were obtained using a Hitachi 4300 SE/N microscope at an accelerating voltage of 10 kV equipped with an Oxford Instruments INCA X-MAX energy-dispersive X-ray spectroscopy (EDS) system with a 80 mm^2 silicon drift detector. To improve conductivity, samples were sputter coated with carbon prior to imaging and EDS analysis. The edge-on image in Fig. 1(a) clearly shows the presence of two distinct regions: a thin layer of ceria deposited on top of the bulk alumina substrate. A film thickness of 272 ± 6 nm (95% C.I.) was obtained by collecting 15 separate measurements at different locations of the sample. The EDS analysis (Fig. 1(b)) highlights the compositional difference between the alumina substrate and the deposited ceria thin film. These compositional changes are minor with the only noteworthy difference being the presence of L-series cerium peaks on the sample surface, indicating successful deposition of a thin-film of ceria. The X-ray diffraction pattern of the oxidized sample is shown in Fig. 1(c). The major peaks of α-Al_2O_3 are clearly visible in addition to peaks indicating the presence of the fluorite-phase CeO_2.

Atomic force microscopy (AFM) was used to collect the images shown in Fig. 2. A 5 × 5 μm2 measurement (Fig. 2(a)) found the manufacturer's estimate of the substrate roughness to be conservative, Ra = 8.18 nm. Measurements of the as-deposited film (Fig. 2(b)) show an arithmetic average roughness slightly less than that of the substrate Ra = 5.34 nm. Arithmetic average roughness values for the oxidized and reduced samples were found to be 11.1 nm and 19.7 nm, respectively. The increase in surface roughness is characterized by the appearance of cracks in the film after oxidation (Fig. 2(c)) and the growth of those cracks after reduction (Fig. 2(d)). It is plausible that removal of oxygen from the reduced film further exacerbated stresses in the film resulting in larger cracks.

The characterization techniques described above are used to obtain accurate estimations of the properties of the ceria thin film for characterization by VASE. SEM imaging provides an estimate for film thickness and AFM is used to determine the surface roughness; both are important parameters in the VASE model fits. EDS and XRD confirm the expected composition and phase identity of the solid system, as shown in Figs. 1(b) and 1(c).

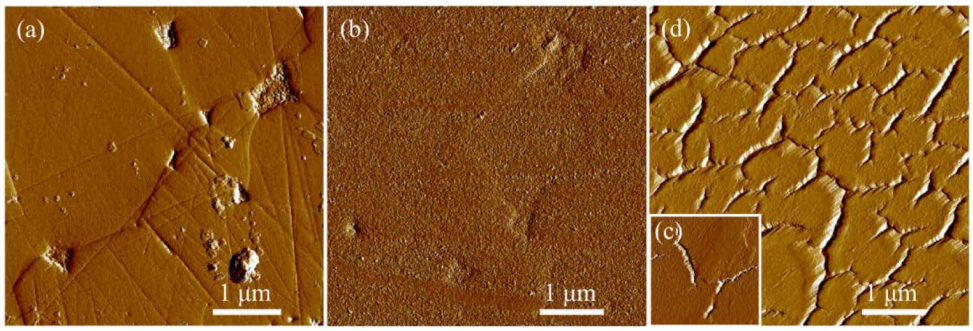

Fig. 2. Atomic force microscopy images. (a) The alumina substrate (a) As-deposited ceria thin film surface. (c) Ceria film after reduction at 1265°C. (d) Sample surface after oxidation at 600°C and before the reduction step.

Optics EXPRESS

2.3 Variable angle spectroscopic ellipsometry

A JA Woollam M-2000D ellipsometer was used to collect ellipsometric data for the oxidized and reduced samples at 50°, 55°, 60°, 65°, and 75° over the 193–1690 nm spectral range. VASE measures the ellipsometry parameters Ψ and Δ. Refractive indices, $m = n - ik$, are extracted by fitting a predicted Ψ and Δ from an exact solution of Maxwell's equations for a plane wave incident on a stack of optically-distinct layers. A set of thicknesses and dispersion models of all layers are referred in this study as the ellipsometric model. Unknowns defining the model—such as the layer thickness or a Lorentz oscillator amplitude—are determined by fitting the model predictions to the measured data using a least-squares fitting algorithm. Description of the ellipsometric model employed in the present study can be split into two parts: the geometric part that describes the layer and effective layer thicknesses and the dispersion part that describes the optical response of the ceria layer to an electromagnetic wave excitation.

The geometric model that best fits the ellipsometry parameters over the measured spectral range is shown in Fig. 3(a) consisting of an alumina substrate layer, an intermix layer, a solid ceria layer, and a top roughness layer. The roughness and intermix layers use Bruggeman's rule to model the layer as 50% each of the materials by volume above and below it where a void layer is assumed above the roughness layer. The film thickness determined from VASE agrees well with the thickness determined from the SEM images with thicknesses of 301.7 and 266.1 nm for the oxidized and reduced samples, respectively. The reduced sample falls within the 95% confidence interval of the sample thickness measured using SEM images while the oxidized sample was found to be slightly thicker. The electron beam physical vapor deposition is a line-of-sight method and no effort was made to control uniformity of the films deposited simultaneously on the 25 samples arranged on the sample holder over an area about 70 × 50 mm^2. A 30 nm variation between films at two different locations for the deposition process is within reason. Roughness layer thicknesses agreed with those measured by AFM: 12.5 and 23.3 nm for the oxidized and reduced samples, respectively. The intermix layer of ceria and alumina was found to be larger than the roughness of the substrate measured by AFM, 24.7 nm and 48.9 nm for the oxidized and reduced samples, respectively. We suspect solid diffusion of the substrate into the film and vice versa is possible at the high temperatures the samples were exposed to during heat treatment and may explain a layer this size. The growth of the intermix layer in the reduced sample, which underwent a longer and higher temperature thermal treatment, is consistent with this suspicion.

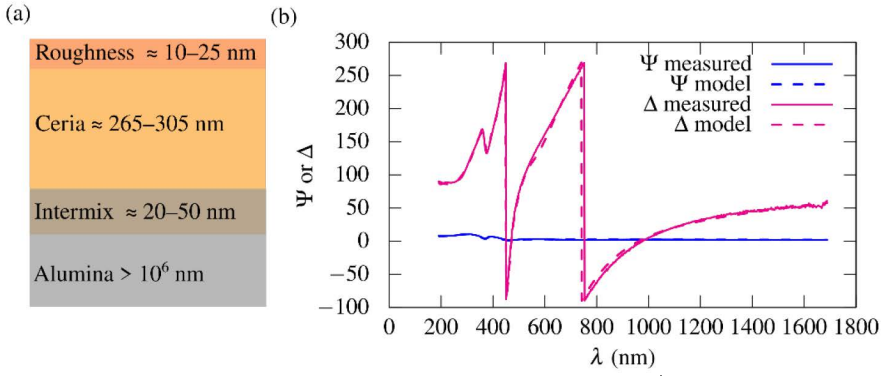

Fig. 3. Determination of refractive index by VASE. (a) Geometric model used to predict the refractive index of oxidized and reduced ceria. (b) Exemplary raw Ψ and Δ data from VASE experiments at an angle of 60° for the oxidized ceria films showing good agreement with model predictions.

Optics EXPRESS

There is no agreed-upon dispersion model to describe the behavior of ceria in the literature. Patsalas and associates studied nanocrystalline ceria and found that the use of two Tauc–Lorentz oscillators fit their ellipsometric data well and predicted a reasonable band gap [8]. Balakrishnan and associates also studied nanocrystalline ceria films with VASE but used a Forouhi–Bloomer model to fit their data [10]. Guo used a modified Lorentz oscillator model with four oscillators to describe crystalline and amorphous ceria films [9]. In the present work, we adopt a model developed by Likhachev and associates to describe semiconductors with absorption features below the band gap [17]. The model is similar to the one used by Patsalas and associates [8], but allows the sub-band gap features found in our films to be adequately modeled using Lorentz and Gaussian oscillators. Like their model, two Tauc–Lorentz oscillators centered at ~4 eV and ~8 eV were found to represent some features of the data well. To capture all features of the data, however, two more Lorentz oscillators centered at 3 eV (400 nm) and 2.3 eV (550 nm) were necessary to obtain a good fit to the ellipsometric data for the oxidized ceria sample as discussed shortly. The same was found to be true for the reduced sample, but an additional Lorentz oscillator—presumably due to reduction of the film—located near 1.35 eV (900 nm) was found to be necessary to fit the ellipsometric data. The band gaps predicted by the fitting procedure to the model were 3.1 and 2.9 eV for the oxidized and reduced samples, respectively. These values are in agreement with those found in the literature, and the reduced band gap energy with higher concentrations of Ce^{+3} (more reduction) has been reported previously [8,15]. The films were found to have a slightly graded (between 4.5 and 7.5% variation) in the real part of the refractive index, likely due to a change in film density as it was deposited. Previous work on the optical characterization of ceria films showed the refractive index to vary linearly with density [8].

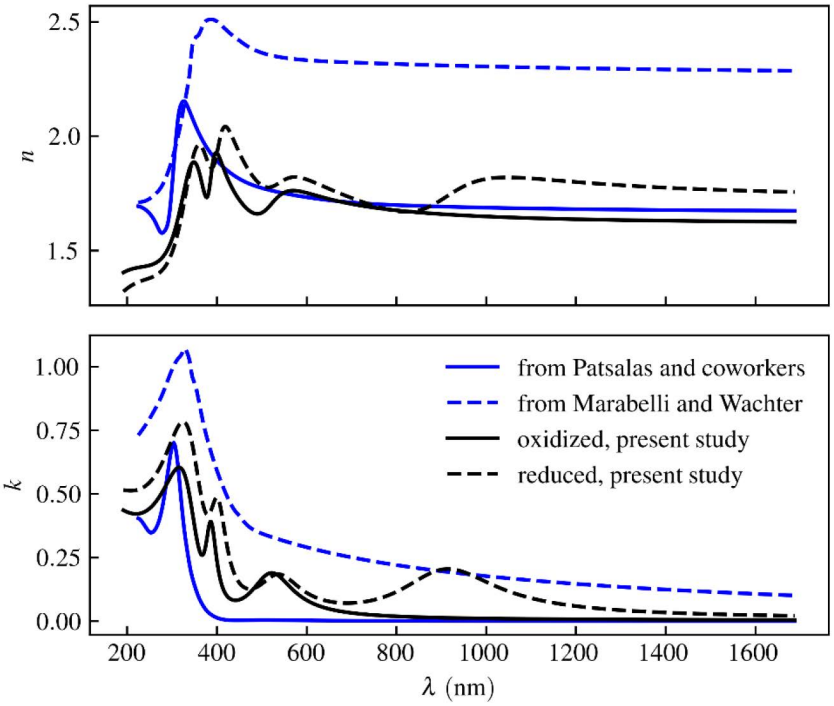

Fig. 4. The real and imaginary part of the refractive index as measured using VASE for an oxidized and a non-stoichiometrically reduced film of ceria. Refractive index data determined for nano-crystalline thin ceria films from Patsalas and associates [8] and for a single crystal of reduced ceria from Marabelli and Wachter [15] are also included.

Optics EXPRESS

After fitting, the model captures all features of the ellipsometric data. The mean squared error per angle between the model and ellipsometric data is less than 3 for both cases, well within the acceptable range [18]. Model degrees of freedom were removed when found to be highly correlated with other fitted variables until the entries in the correlation matrix were all less than 0.4 Exemplary raw data for an incidence angle of 60° is shown in shown in Fig. 3(b). Similar agreement can be shown for other angles. The refractive indices of the alumina substrate were determined first using a bare substrate and were assumed to stay constant through the deposition and heat treatment processes.

The calculated real and imaginary parts of the refractive index based on VASE measurements for the oxidized and reduced samples are shown in Fig. 4. Refractive index data from Patsalas and associates [8] and Marabelli and Wachter [15] have also been included in the figure for reference. Patsalas and associates studied stoichiometric nanocrystalline ceria films with up to 10% Ce_2O_3 content using VASE. This data will be referred to as the reference data in the following text. Marabelli and Wachter characterized a reduced ceria sample using optical reflectivity measurements, but the reduction state of the sample was not identified. It was likely in a reduction state beyond the reach of the solar thermochemical systems motivating the present study since they were heated to 2275°C for two hours. These two data sets demonstrate the wide variation in optical properties reported in the literature for ceria due to differences in material composition/morphology or (possibly) the characterization approach. Indeed, the refractive index of ceria for deposited films has been shown to be strongly dependent upon substrate temperature during deposition [8,10,19]. Including data from other studies, such as the one by Guo and associates [9], would further strengthen this point. The magnitudes of the real and imaginary components of the refractive index identified by this study fall within range of existing data.

There are two additional absorption peaks centered around 400 and 550 nm that appear in the acquired imaginary part of the refractive index but do not appear in the data from [8] and [15]. These peaks have been identified previously using photoluminescence measurements of ceria thin films [20]. The peak at 400 nm was attributed to the existence of Ce_6O_{11} in the film after annealing at high temperatures. This phase could be present in the films presently under study, but would require a high resolution XRD measurement near $2\theta = 59$ degrees to differentiate the characteristic peak from the CeO_2 peak shown in Fig. 1(c). The peak near 550 nm was attributed to oxygen-related defects.

The complex part of the refractive index for the reduced sample retains the same qualitative behavior as the oxidized sample up to 600 nm. The increase in absorption for the reduced sample for the spectral range $\lambda < 450$ nm can be attributed to a broadening of the peak located near 400 nm attributed to the existence of Ce_6O_{11} in the film. Indeed, the peak was previously observed only after thermal treatment of the ceria sample after a rapid thermal annealing in argon at 1000°C for 5 minutes [20]—a treatment similar to the reduction step carried out in the current study. The most notable difference between the imaginary part of the refractive index of the oxidized and reduced samples is the broad absorption that appears in the near IR region for the reduced sample. This explains the blackened color of the electron beam targets noted in the previous subsection. We believe this peak is solely due to the oxygen deficiency of the film.

3. Mathematical model of an aerosolized ceria particle undergoing solar-driven thermochemical reduction

The model we present here is simple enough to clearly demonstrate the importance of the chemical state on the energy and mass transfer to and from ceria, but complete enough to include the important mechanisms present in a directly irradiated dilute fluidized bed reactor. We consider a single spherical ceria particle with radius r entrained in a flow of argon under direct solar irradiation from a solar concentrator. The particle undergoes the endothermic, non-stoichiometric reduction given by Eq. (1). Concentrated solar irradiation brings the

particle to high temperatures and, in turn, drives reduction. The critical radiative property that decides how effectively the radiative energy is delivered to the particle is the absorption efficiency factor. It exhibits behavior important enough to warrant its own section.

3.1 Conservation of mass and chemical kinetics

We define a control volume around the particle and assume that oxygen leaves the control volume as a gas as soon as it is produced,

$$\frac{\mathrm{d}M_{\mathrm{O}_2}}{\mathrm{d}t} = \frac{4}{3}\pi r^3 \frac{\delta}{2} r_{\mathrm{c}} - \dot{m}_{\mathrm{O}_2} = 0. \tag{2}$$

Here M_{O_2} is the total moles of oxygen in the control volume, r_{c} is the reaction rate, and $\dot{m}_{\mathrm{O}_2}$ is the molar flow rate out of the control volume.

Recent work by Bulfin and associates developed a reaction rate expression for ceria reduction and oxidation in terms of the non-stoichiometry [21]. The expression takes on the general appearance of a first-order reaction in both directions with an Arrhenius term to account for temperature dependence:

$$\frac{\mathrm{d}\delta}{\mathrm{d}t} = (x-\delta) A_{\mathrm{red}} e^{\frac{-\bar{E}_{\mathrm{red}}}{\bar{R}T}} - \delta p_{\mathrm{O}_2}^{\nu} A_{\mathrm{ox}} e^{\frac{-\bar{E}_{\mathrm{ox}}}{\bar{R}T}}. \tag{3}$$

In Eq. (3), x is the maximum non-stoichiometry, $A_{\mathrm{red/ox}}$ is a frequency factor, $\bar{E}_{\mathrm{ox/red}}$ is an activation energy, ν is dimensionless constant, $\bar{R}$ is the gas constant, p_{O_2} is the partial pressure of oxygen in the carrier gas, and T is the particle temperature. We assume a uniform temperature of the particle as justified by Biot numbers satisfying Bi<0.01 for the radii and thermal conductivities considered here. The meanings, values, and sources for the constants appearing in Eq. (3), and the equations that follow, are summarized in Table 1. The reaction rate appearing in Eq. (2) can be expressed in terms of the non-stoichiometry by introducing the concentration of ceria, $r_c = \dot{\delta}[\mathrm{CeO}_2]$ where the dot indicates a time derivative. Thus, solution to Eq. (3) will yield a transient molar flow rate of oxygen when combined with Eq. (2).

3.2 Conservation of energy

The energy balance of the control volume takes into consideration the input of flux, the net heat transfer used to drive the endothermic reaction, and the energy leaving the control volume with the oxygen. A lengthy derivation, as can be found in [26], yields:

$$\bar{M}_{\mathrm{CeO}_2} \bar{c}_p(\delta) \frac{\mathrm{d}T}{\mathrm{d}t} = \dot{Q} - \dot{m}_{\mathrm{O}_2} \Delta\bar{H}(\delta) - \dot{m}_{\mathrm{O}_2} \bar{R} T. \tag{4}$$

Here $\bar{M}_{\mathrm{CeO}_2}$ is the molar mass of ceria, $\bar{c}_p$ is the heat capacity per mole at constant pressure, T is the particle temperature, $\dot{Q}$ is the net heat transfer to or from the particle, and $\Delta\bar{H}$ is the reaction enthalpy as a function of non-stoichiometry. To arrive at Eq. (4), we have assumed the oxidized and reduced ceria have similar molar mass. The molar heat capacity at constant pressure, however, is adjusted according to the reduction state, $\bar{c}_p = \bar{c}_{p_{\mathrm{red}}}\delta + \bar{c}_{p_{\mathrm{ox}}}(1-\delta)$.

The heat transfer mechanisms considered in the model are: heating due to absorption of the incident solar irradiation, thermal radiative emission, and conduction to or from the carrier gas,

Optics EXPRESS

Table 1. Physical quantities and sources of data used for ceria and argon in the present study.

Quantity	Description	Value	Units	Source
x	Maximum non-stoichiometry	0.35	–	[21]
v	Reaction exponent	0.218	–	[21]
$\bar{E}_{red}$	Reduction activation energy	232,000	J mol^{-1}	[21]
$\bar{E}_{ox}$	Oxidation activation energy	36,000	J mol^{-1}	[21]
A_{red}	Reduction frequency factor	720000	s^{-1}	[21]
A_{ox}	Oxidation frequency factor	82	s^{-1} bar^{-v}	[21]
$\bar{M}$	Molar mass of argon	39.94	g mol^{-1}	[22]
$\bar{R}$	Universal gas constant	8.314	kJ kmol^{-1} K^{-1}	[22]
α	Thermal accommodation coefficient	1	–	[23]
γ	Specific heat ratio of argon	3/2	–	[23]
$\bar{c}_p$	Heat capacity per mole of ceria	interpolated	J K^{-1} mol^{-1}	[24]
k	Thermal conductivity of carrier gas	interpolated	W m^{-1} K^{-1}	[25]
$\Delta\bar{H}(\delta)$	Enthalpy change with non-stoichiometry	interpolated	J mol^{-1}	[16]
[CeO_2]	Concentration of solid ceria	41.919	kmol m^{-3}	[14]
p	Total gas pressure surrounding the particle	1	atm	N/A
p_{O2}	Partial pressure of oxygen in the carrier gas	10^{-4}	bar	N/A

$$\dot{Q} = \dot{Q}_{abs} - \dot{Q}_{emit} - \dot{Q}_{cond}. \quad (5)$$

The power absorbed by the irradiated particle is given by

$$\dot{Q}_{abs} = \pi r^2 \int_0^\infty Q_{abs} C G_{sol} d\lambda, \quad (6)$$

where C is the concentration ratio, Q_{abs} is the absorption efficiency factor of the particle, G_{sol} is the solar irradiation given by the ASTM air mass 1.5 solar spectrum [27], and the integration interval is over all wavelengths. The thermal emission from the particle is calculated as

$$\dot{Q}_{emit} = (\pi r^2) \int_0^\infty Q_{abs} E_{b\lambda}(T) d\lambda, \quad (7)$$

where $E_{b\lambda}(T)$ is Planck's blackbody function evaluated at the temperature T and wavelength λ. Lastly, we account for the energy transfer due to the interaction with the carrier gas.

Particles assumed to be perfectly entrained are found in the solar reactor literature ranging from tens of nanometers [28] to tens of microns [29]. For particles size on the order of the mean free path of the gas, sub-continuum effects need to be considered. We use the model by Fuchs, as described in the work of Daun and Huberman [23], to simulate conductive transfer spanning the continuum to sub-continuum regimes. The power delivered to or lost by the particle is given by

$$\dot{Q}_{cond} = 4\pi(r + \Delta) k (T_\Delta - T_\infty). \quad (8)$$

According to the model, we assume there exists a shell of rarefied gas surrounding the particle at a temperature T_Δ and a continuum background gas at temperature T_∞. The shell is assumed to be in the free molecular regime and to have a thickness equal to the mean free path, Δ. We use expression from [30] to evaluate the mean free path of a monatomic gas:

Optics EXPRESS

$$\Delta = \frac{4}{5}\left(\frac{Tk(T)}{p}\sqrt{\frac{\bar{M}}{2k_{\mathrm{B}}T}}\right). \tag{9}$$

The thermal conductivity k appearing in (8) is that of the gas averaged over the temperature range defined by T_Δ and T_∞. Expressions for heat transfer rates between a spherical solid surface and a gas in the free molecular regime and the continuum regime are well established. By imposing that energy is conserved at the interface of the rarefied sphere and the continuum, we obtain an expression that can be solved for T_Δ by equating the two expressions,

$$4\pi(r+\Delta)k\left(T_\Delta - T_\infty\right) = \alpha\pi r^2 p\sqrt{\frac{2k_{\mathrm{B}}N_{\mathrm{A}}T_\infty}{\pi\bar{M}}}\frac{\gamma+1}{\gamma-1}\left(\frac{T}{T_\Delta}-1\right), \tag{10}$$

where α is the accommodation coefficient and p is the total pressure of the carrier gas. The thermal conductivity is again averaged over the temperature range. k_{B}, N_{A}, $\bar{M}$ and γ are Boltzmann's constant, Avogadro's number, the molar mass of the carrier gas, and the specific heat ratio, respectively. The parameter values used in this study can be found in Table 1. When the mean free path of the gas is much smaller than the particle size, the expected continuum behavior is recovered and (8) becomes the familiar Newton's law of cooling.

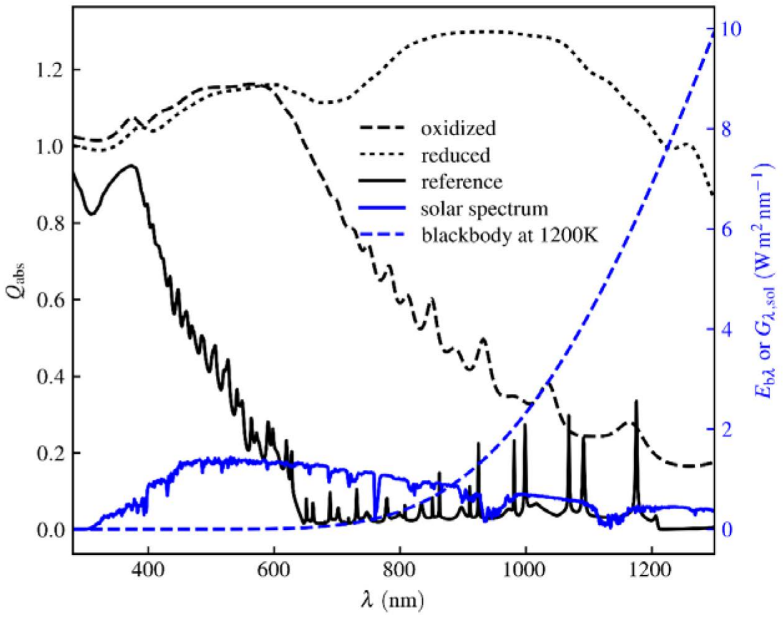

Fig. 5. Absorption efficiency factor for a 1 μm radius spherical ceria particle for three different refractive indices: determined from the oxidized and reduced samples in this work, and the reference data from Patsalas [8]. The air mass 1.5 solar spectrum ($G_{\lambda,\mathrm{sol}}$) and blackbody emission at 1200 K ($E_{\mathrm{b}\lambda}$) are also shown.

Optics EXPRESS

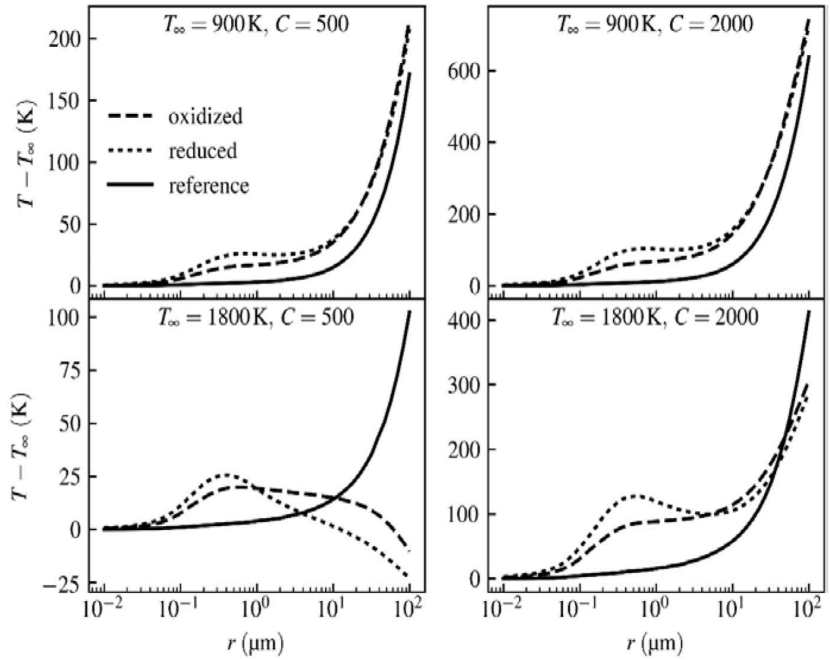

Fig. 6. Difference in steady-state particle temperature from free stream temperature for four different choices of T_∞ and C.

3.3 Thermal radiative properties

The radiative properties of the spherical ceria particle were obtained using the Lorenz–Mie solution to Maxwell's equations and the widely adopted code provided by Bohren and Huffman [31]. The pertinent property for thermal transport is the absorption efficiency factor. The spectra for a 1 μm radius particle of ceria made of the oxidized and reduced samples are shown along with the results for the reference ceria data in Fig. 5. The importance of the broad spectral increase in the complex part of the refractive index of the reduced sample is now clearly seen. The absorption efficiency factor is many times larger than the oxidized and reference particles in the near IR part of the spectrum.

Since the steady-state particle temperature is a result of a trade-off between radiative emission and absorption, the identified difference in absorption efficiency factor is anticipated to significantly impact the solution to Eq. (4). If one neglects the conduction heat transfer in Eq. (4), the steady-state temperature results from radiative processes only. Since the reduced particle emits strongly in the near IR, the onset of strong blackbody emission is experienced by the particle at lower temperatures than the oxidized and reference ceria particles, leading to the lowest steady-state temperature. The reference ceria particle behaves like a selective solar absorber, absorbing only short-wavelength radiation while little thermal emission occurs at wavelengths longer than 650 nm because of a very low absorption efficiency factor in this spectral region. Consequently, the reference ceria particle attains the highest steady-state temperature. These assertions have been borne out by numerical solutions not included in this work for brevity.

Optics EXPRESS

4. Thermochemical model results

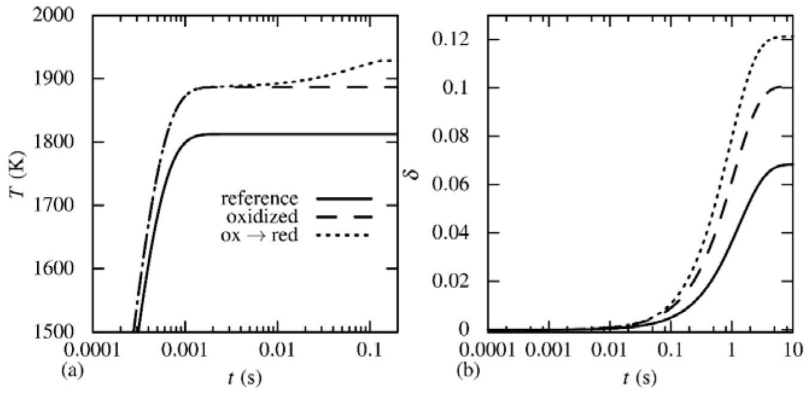

Fig. 7. Transient simulation results for an aerosolized ceria particle undergoing reduction with three different assumed radiative behaviors.

First, we consider steady-state predictions of the presented model—Eq. (5) set to zero. In steady-state, the non-stoichiometry goes to the thermodynamic equilibrium value which can be determined from the particle temperature and the prescribed partial pressure of oxygen of the background gas. Of the three free parameters appearing in Eqs. (5)–(8), the particle radius is the most influential since it is integral to the determination of all three terms in Eq. (5). Here we present results for the steady-state temperature against radius for four different choices of concentration ratio and free stream temperature. For the concentration ratio we consider values of 500 and 2000, a low and high value in the range achievable by a power tower heliostat field configuration, respectively [32]. The two cases of free stream temperature are chosen to be 900 K and 1800 K. These temperatures are representative of those reached during oxidation and reduction, respectively, in a recent experimental study [4]. The choice of total pressure of the gas surrounding the particle as 1 bar is also motivated by this study. Results for all four possible permutations of of free stream temperature and concentration ratio over a range of particle radii are shown in Fig. 6. The range of particle radii chosen is representative of those already studied in the thermochemical reactor modeling literature [28,29]. Each row represents a choice for T_∞ while each column represents a choice for C. The temperature shown is the departure from the free stream temperature. One immediate conclusion can be made by looking at the figure: changes in radiative properties, particularly in the IR, can dramatically change the thermal behavior of the particles.

For T_∞ = 900 K, the steady state temperature follows the same qualitative behavior for both concentration ratios as shown in Figs. 6(a) and 6(b). When the particle is too small, conduction dominates the energy balance, and the temperature does not appreciably depart from the free stream temperature. As the particle grows, absorption efficiency factor increases with radiation wavelength enhancing absorption while the surface area of the particle relative to its volume shrinks until the magnitude of conduction heat transfer approaches that of radiation and the particle rapidly increases its temperature above the free stream temperature. This transition is easily observed in Figs. 6(a) and 6(b) near 10 μm. The subcontinuum heat transfer due to conduction described by Eq. (8) is important for particles sizes ranging from 0.1 to 10 μm. A distinct hump is visible in this range where the effect of the difference in radiative properties is enhanced by the decreased conductive heat transfer. Predictions for steady-state temperatures in this range differ by as much as 38°C between the oxidized and reduced particles. The difference between the reference particles and reduced particles is even greater: 98°C. For total pressures closer to atmospheric pressure, this behavior disappears.

Optics EXPRESS

The higher free-stream temperature case of 1800°C is shown in Figs. 6(c) and 6(d). For lower concentration ratio, some unexpected behavior is observed; the particles may come to equilibrium at a temperature lower than the free-stream temperature. That is, for the sufficiently high free-stream temperature, the particle is heated to temperatures corresponding to very large thermal emission. Consequently, radiative cooling occurs. The effect is strongest for the ceria particles with the strongest absorption (emission) in the infrared region where the blackbody emissive power is highest. This corresponds to reduced ceria as is clearly shown in Figs. 6(c). Radiative cooling does not occur for particles irradiated with a concentration ratio of 2000. As with the lower free stream temperature, the influence of subcontinuum heat transfer is again clearly seen in Figs. 6(c) and 6(d) with a distinct feature located between particles sizes 0.1 and 10 μm. The highest difference in steady-state temperature is achieved in this range where the difference between the reduced ceria and the oxidized ceria is as high as 42°C. The difference between the reference ceria and the reduced ceria case is over 100°C.

A complete transient solution to Eqs. (3) and (4)—governing the transient temperature and reduction extent of the particle—is shown in Fig. 7 for a 0.6 μm particle irradiated by 2000 suns in a 1550 K carrier gas with an oxygen partial pressure of 10^{-4} bar. Three cases are shown: the particle is made up the reference ceria and the refractive index is constant; the particle is made up of oxidized ceria and the refractive index is constant; and the particle is made up of ceria whose refractive index is a function of non-stoichiometry. The latter case is accomplished by assuming a linear interpolation between the oxidized and reduced refractive indices presented in the current work. The full approach to steady state is shown in Figs. 7(a) and 7(b). The kinetics are clearly the reaction limiting factor here as the particle heats up rapidly on a time scale much faster than the chemical changes. The effect of accounting for refractive index changes with reduction extent is clearly seen in Fig. 7(a) between 0.01 s and 0.1 s. An particle appears to reach a steady temperature at 0.001 s, then gradually increases as the lagging kinetics lead to chemical—and therefore radiative—changes. Differences in steady-state temperature lead to differences in steady-state predictions of the non-stoichimetry of 0.02 between the oxidized and reduced particles, a 20% relative difference. The difference in non-stoichiometry between the reference and reduced case is even higher, 0.05.

The trend observed in the case shown in Fig. 7—that the kinetics are far slower than the heat transfer—holds true for most of the particle sizes considered in this study. Figure 8 shows the time for the particle temperature and non-stoichiometry to reach steady state (the settling time) versus particle size for a partial pressure of oxygen and solar concentration ratio of 10^{-4} bar and 2000, respectively. Settling times for temperature are orders of magnitude higher than for the non-stoichiometry coefficient for particle sizes up to almost 1 μm. Thus the time to reach a steady reduction state is essentially constant for these particle sizes. The time to full reduction extent is only influenced by heat transfer rate when particles are large. Bigger particles have higher thermal mass and smaller surface area per volume reducing the importance of conductive transfer. These observations are in line with previously reported trends on ceria characteristic size and reduction times [6].

Optics EXPRESS

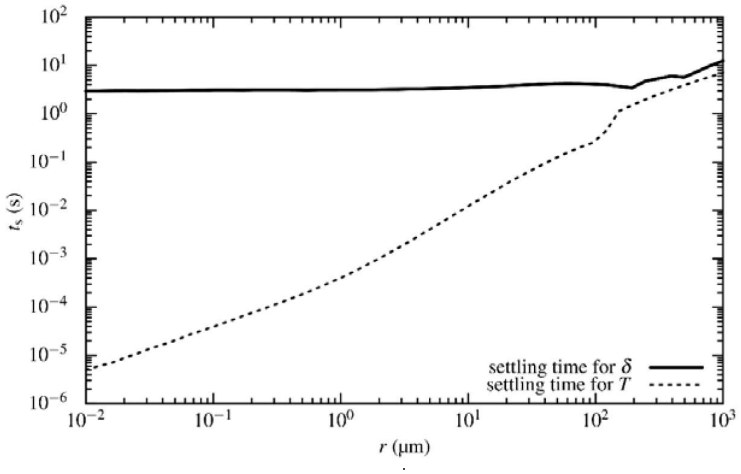

Fig. 8. Thermal and chemical settling times vs particle radius for a ceria particle undergoing reduction.

5. Summary and conclusions

The complex refractive index of ceria for fully oxidized and partially reduced ceria has been determined at room temperature over the spectral range 193–1690 nm by performing variable angle spectroscopic ellipsometry on thin films deposited by electron beam physical vapor deposition. Auxiliary experiments to determine the roughness, thickness, and chemical composition of the films corroborate the ellipsometric model used to extract the radiative parameters. A model of an aerosolized particle undergoing solar-driven, non-stoichiometric reduction was solved to demonstrate the potentially large differences in equilibrium temperatures and non-stoichiometries predicted for solar thermochemical reaction systems based on ceria caused by neglecting the chemical dependence of the radiative properties on reduction state. Equilibrium temperatures differing by hundreds of degrees were found in the cases under study motivated by realistic estimates for operating pressures, temperatures, and concentration ratios.

Two major conclusions are drawn from this work. Firstly, the radiative properties of ceria change significantly when it is non-stoichiometrically reduced. It absorbs more light in the optical and near infrared spectral ranges. Secondly, this behavior has practical implications: models used to help design high temperature, solar-driven thermochemical reactors based on ceria could greatly misrepresent the radiative—and, therefore, thermal and chemical—performance of the system.

Funding

Australian Research Council (FT140101213).

Acknowledgments

This work was performed in part at the ACT node of the Australian National Fabrication Facility, a company established under the National Collaborative Research Infrastructure Strategy to provide nano and micro-fabrication facilities for Australia's researchers. The authors would like to thank Mr. Ankur Sharma for the AFM measurements of thin film ceria samples and Dr. Mykhaylo Lysevych for help with the film deposition. This work was contributed to the 2017 OSA Light, Energy, and the Environment Conference in 2017 (paper RTh2B.6) and the Eurotherm Seminar No. 110 (2018).